Hierarchically structured carbon electrodes derived from intrinsically microporous Tröger's base polymers for high-performance supercapacitors

Journal Pre-proofs

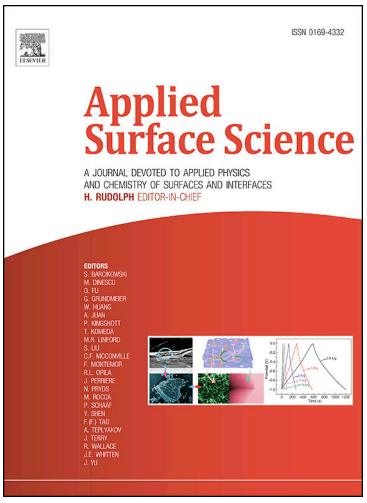

Hierarchically structured carbon electrodes derived from intrinsically microporous Tröger's base polymers for high-performance supercapacitors

Jun Woo Jeon, Joobee Shin, Jinyoung Lee, Ji-Hoon Baik, Richard Malpass-Evans, Neil B. McKeown, Tae-Ho Kim, Jong-Chan Lee, Sung-Kon Kim, Byoung Gak Kim

PII: S0169-4332(20)31903-6
DOI: https://doi.org/10.1016/j.apsusc.2020.147146
Reference: APSUSC 147146

To appear in: *Applied Surface Science*

Received Date: 7 May 2020
Revised Date: 24 June 2020
Accepted Date: 30 June 2020

Please cite this article as: J. Woo Jeon, J. Shin, J. Lee, J-H. Baik, R. Malpass-Evans, N.B. McKeown, T-H. Kim, J-C. Lee, S-K. Kim, B. Gak Kim, Hierarchically structured carbon electrodes derived from intrinsically microporous Tröger's base polymers for high-performance supercapacitors, *Applied Surface Science* (2020), doi: https://doi.org/10.1016/j.apsusc.2020.147146

Hierarchically structured carbon electrodes derived from intrinsically microporous Tröger's base polymers for high-performance supercapacitors

Jun Woo Jeon[a,1], Joobee Shin[b,1], Jinyoung Lee[a], Ji-Hoon Baik[a], Richard Malpass-Evans[c], Neil B. McKeown[c], Tae-Ho Kim[a], Jong-Chan Lee[d,*], Sung-Kon Kim[b,*], Byoung Gak Kim[a,e,*]

[a]Advanced Materials Division, Korea Research Institute of Chemical Technology (KRICT), 141 Gajeong-ro, Yuseong-gu, Daejeon 34114, Republic of Korea. E-mail: bgkim@krict.re.kr

[b]School of Semiconductor and Chemical Engineering, Jeonbuk National University, 567 Baekje-daero, Deokjin-gu, Jeonju-si, Jeollabuk-do 54896, Republic of Korea. E-mail: skkim@jbnu.ac.kr

[c]EaStChem School of Chemistry, University of Edinburgh, Edinburgh, UK.

[d]School of Chemical and Biological Engineering, Institute of Chemical Processes, Seoul National University, 1, Gwanak-ro, Gwanak-gu, Seoul 088026, Republic of Korea.

[e]Department of Chemical Convergence Materials, University of Science and Technology, 217 Gajeong-ro, Yuseong-gu, Daejeon 34113, Republic of Korea.

Abstract

Three-dimensional (3D) hierarchically porous carbons have been extensively investigated as their large surface area and facile ion transport can provide high-performance in energy applications. Here we report new hierarchically porous carbon materials based on a polymer of intrinsic microporosity (PIM composed of ethanoeanthracene (EA) by Tröger base (TB) components (PIM-EA-TB)), for use in high-performance supercapacitor electrodes. Hierarchically structured carbon was prepared from nonsolvent-induced phase separation (NIPS) and subsequent carbonization. The intrinsic micropores of PIM-EA-TB and meso- and macro-pores formed via the NIPS process imbue the resulting carbon material with a hierarchical porous architecture with an exceptionally high surface area of 1966 m^2 g^{-1} and a high electrical conductivity of 83.6 S cm^{-1}. This well-organized structure provides pathways for efficient charge transportation, giving it a high specific capacitance of 46 F g^{-1} at 1 A g^{-1} and an excellent specific energy of 17 W h kg^{-1} at a specific power of 1 kW kg^{-1}.

Keywords : Polymers of intrinsic microporosity, Supercapacitor, Micropore, Hierarchical structure, Tröger's base polymer

1. Introduction

Supercapacitors (SCs), which are also known as electrochemical capacitors, have gained attention as promising energy storage devices that are capable of managing high power densities and have excellent cycle life, wide working temperature ranges, and good operational safety, allowing them to bridge the gap between batteries and conventional electrolytic capacitors [1-8]. These features are attributed to their charge storage mechanism, which is based on charge accumulation at the electrode/electrolyte interface [5, 9]. However, this mechanism limits the energy densities of SCs, which are typically only a tenth of those of conventional rechargeable batteries.

To achieve better SC performance, particularly with respect to capacitance and energy density, porous carbon materials including activated carbons (ACs), carbon nanotubes (CNTs), carbon aerogels, and graphene have been extensively studied due to their high electrical conductivity and ion-accessible surface area [10-13]. However, some reports have indicated that carbon nanomaterials that have only micropores can exhibit poor wetting of the electrode by the electrolyte ions, resulting in poor electrochemical performance [14, 15]. To overcome this issue, the use of three-dimensional (3D) hierarchical porous carbon materials with micro-, meso-, and macropores has frequently been suggested. Such trimodal pores provide a large surface area, good wetting, and suitable transport paths for both ions and electrons [16, 17]. Various 3D hierarchically structured carbons with well-defined pores and high electrical conductivity have been prepared for high-performance SCs [15, 18-24]. For example, Xu et al. reported that a 3D holey graphene framework with a hierarchically porous structure delivered

an excellent gravimetric capacitance of 298 F g^{-1} and volumetric capacitance of 212 F cm^{-1} in an organic electrolyte [25]. We recently reported another successful example of nanostructuring, in which hierarchically structured porous carbon electrodes based on a polymer of intrinsic microporosity (PIM-1) were used to produce high-performance SCs [16]. PIM-1 exhibited a large specific surface area of 800 m^2 g^{-1}, which was mainly derived from inherent micropores less than 1 nm in size. Surprisingly, the carbonized material showed an enhanced specific surface area of ~2100 m^2 g^{-1} and high electrical conductivity, while retaining its <1 nm micropores. Furthermore, meso- and macropores were simultaneously formed in the microporous PIM-1 matrix via nonsolvent-induced phase separation (NIPS) techniques, which allowed easy access of the electrolytes to the micropore regions. Benefiting from these attributes, the PIM-1-based hierarchically structured carbons delivered an excellent specific energy of 43.2 W h kg^{-1} at a specific power of 1.25 kW kg^{-1}.

Based on the molecular design flexibility, solution processability, and intrinsic microporosity (which is retained or enhanced after carbonization) of PIMs, carbon materials based on PIMs have recently been investigated for use in energy and environmental applications [26-31]. PIM-EA-TB consisting of ethanoeanthracene (EA) and Tröger's base (TB) units, have shown potential in gas separation and energy storage applications due to their higher intrinsic specific surface area (>1000 m^2 g^{-1}) and rigidity as compared to PIM-1 [26, 31-35]. Marken et al. reported that PIM-EA-TB based microporous carbons with heteroatoms on their surface, made via a vacuum carbonization process exhibited pH-switchable supercapacitive properties [31]. However, their low electrical conductivity and relatively low surface area of 242 m^2 g^{-1} were not optimised for this application.

In this study, we demonstrate the properties of PIM-EA-TB-based hierarchically porous

carbon materials with high surface areas and electrical conductivity, prepared by NIPS and carbonization at 1100 °C, and tested their performance as SC electrodes. Notably, the resulting carbons showed a high specific surface area of 1966 $m^2 g^{-1}$ and electrical conductivity of 83.6 S cm^{-1} without collapse of their porous structure. The supercapacitive performance parameters of the carbonized PIM-EA-TB materials, including capacitance, rate-retention capability, charge/discharge behavior, and cycle lives are explicitly discussed with a focus on the characteristics of the hierarchically structured carbons.

2. Experimental

2.1. Materials

All reagents used in this study were used as received without further purification unless otherwise noted. Dimethoxymethane (95%), chloroform (≥99.9%), and 1,2-dichlorobenzene (DB, 99%) were purchased from Sigma-Aldrich. Aqueous ammonium hydroxide solution (28–30%, extra pure), methanol (99.5%), and *n*-hexane (95%) were purchased from Samchun chemicals. Trifluoroacetic acid (≥99%) was purchased from Tokyo Chemical Industry Co., Ltd. (TCI). Tetrahydrofuran (THF, stabilized, 99.5%) was purchased from J.T. Baker.

2.2. Preparation of materials

2.2.1. Synthesis of PIM-EA-TB

PIM-EA-TB was prepared by the method of Carta et al. [32]. Briefly, 2,6(7)-diamino-9,10-dimethyl-9,10-dihydro-9,10-ethanoanthracene [32]; dimethoxymethane (20.1 mL, 226.9 mmol) was added to 2,6(7)-diamino-9,10-dimethyl-9,10-dihydro-9,10-ethanoanthracene (12.0

g, 45.4 mmol) under a nitrogen atmosphere, and the solution was placed in an ice bath to lower its temperature. Trifluoroacetic acid (100.0 ml) was added dropwise over 30 min. The resulting mixture was stirred for 72 h at room temperature, producing a viscous solution. The solution was then precipitated in 17 wt% aqueous ammonium hydroxide solution, and the precipitate was filtered and washed with water and acetone three times, respectively. The crude polymer was dissolved in chloroform and reprecipitated from methanol three times, redissolved in chloroform, and finally reprecipitated from *n*-hexane to obtain the polymer as a fine powder. The white powder was refluxed for 24 h in methanol and then filtered, followed by rigorous drying in a vacuum oven. Yield: 12.6 g, 92.4%, ^{1}H NMR (500 MHz, $CDCl_3$): δ_H (ppm) = 6.98 (br, m, 4H, Ar *H*), 4.60 (br, s, 2H, N-C*H*$_2$-N), 4.04 (br, s, 4H, N-C*H*$_2$-Ar), 1.79 (br, m, 6H, 2 C*H*$_3$), 1.53 (br, m, 4H, 2 C*H*$_2$). Molar mass: M_n = 32700, M_w= 61900, PDI =1.89. Anal. Calcd for CHN (wt%): C, 83.96; H, 6.71; N, 9.33. Found: C, 79.28; H, 6.42; N, 8.64. BET surface area: 1090 m^2 g^{-1}; total pore volume: 0.66 cm^3 g^{-1} at p/p_0 = 0.99; T_d 5% = 326 °C.

2.2.2. Preparation of hierarchically porous carbon (cNPIM) monolith

The cNPIM-EA-TB monolith was fabricated by the nonsolvent-induced phase separation (NIPS) method and subsequent carbonization. Briefly, PIM-EA-TB powder (1.0 g) was dissolved in a mixture of DB (3.13 g) and THF (12.53 g) at 35 °C with continuous stirring to form a 6 wt% homogeneous solution. The solution was then cast onto a clean flat glass plate with a 300 μm blade gap. The nascent casting solution was immersed in 500 mL of the nonsolvent methanol at room temperature for 24 h. A solid film was formed during the NIPS process. The film was removed from the coagulation bath and dried under ambient conditions

for 48 h. Finally, the film was carbonized in a tube furnace at 1100 °C under an H_2/N_2 atmosphere using a heating rate of 5 °C min^{-1}. The resulting carbon material was referred to as cNPIM-EA-TB. Carbonized PIM-EA-TB (cPIM-EA-TB) was prepared using the same procedure, except that the NIPS process was omitted. In the case of cNPIM-EA-TB, carbonization at 1100 °C with a hold time of 120 or 180 min resulted in 70 and 80% loss of the initial weight, respectively.

2.3. Characterization

The morphologies of the materials were recorded using a field emission scanning electron microscope (FE-SEM, Carl Zeiss (SigmaHD), In-Lens Detector, 10 kV) The Brunauer-Emmett-Teller (BET) surface area and pore size distribution (PSD) were determined from the N_2 adsorption–desorption isotherms at 77 K obtained using a Micromeritics 3Flex instrument. Prior to the BET surface area measurements, the samples were degassed for 30 min at 90 °C and for 24 h at 200 °C. The pore size distribution (PSD) of the carbonized PIM samples was calculated using the Horvath–Kawazoe method. The total pore volume was based on single point adsorption at $P/P_0 = 0.99$. ^1H nuclear magnetic resonance (NMR) spectra of PIM-EA-TB were recorded using a Bruker AVANCE Neo 500 MHz spectrometer in $CDCl_3$. The number-average molecular weight (M_n), weight-average molecular weight (M_w), and polydispersity index (PDI) of PIM-EA-TB were measured using gel permeation chromatography (GPC) in THF using Shodex columns (KF-800 series) at 40 °C. The signals were detected using a Waters 2414 refractive index detector. Elemental analysis was obtained using a Thermo Scientific Flash 2000 Organic Elemental Analyzer equipped with a thermal conductivity detector (TCD).

Thermogravimetric analysis (TGA) was performed to determine the thermal stability of the PIM-EA-TB using TGA Q5000 V3.17 Build 265 from TA Instruments at a heating rate of 10 °C min^{-1} from 25 to 800 °C under a N_2 flow of 35 mL min^{-1}. Fourier transform infrared (FTIR) spectroscopy was carried out using Bruker ALPHA-P and ALPHA-T instruments over the range 4000–400 cm^{-1}. Raman spectra of the carbonized PIM-EA-TBs were acquired using a Renishaw inVia Reflex equipped with a 514 nm Ar-ion laser. XPS measurements were conducted using a Thermo VG Scientific Sigma probe spectrometer equipped with a monochromatic Al Kα source. A four-point probe station was used to measure the electrical properties of the samples. The electrical conductivity of each sample was calculated as follows: $\sigma\ (S\ cm^{-1}) = 1 / (R_{sheet} * t)$, where σ is the conductivity, R_{sheet} is the sheet resistance and t is the thickness of the sample. Electrochemical characterizations, including cyclic voltammetry (CV), galvanostatic charge/discharge (GCD), and electrochemical impedance spectroscopy (EIS), were performed using a SP-200 potentiostat (Bio-Logic, USA) in a two-electrode configuration at room temperature. 1.0 M tetraethylammonium tetrafluoroborate (TEA/BF_4) in acetronitrile (ACN) was used as the electrolyte. The cell assembly and cell tests were carried out in an argon-filled glovebox. EIS was conducted over the frequency range 10^6 kHz–1 Hz at an amplitude of 5 mV. The specific capacitance was estimated from the GCD profiles using the following equation:

$$C=4I/[(\Delta V/\Delta t)m]$$

Where I is the applied current, $\Delta V/\Delta t$ is the slope of the discharge curve after the initial IR drop, and m is the total mass of the two electrodes. The specific power (P, in W kg^{-1}) and energy (E, in Wh kg^{-1}) were calculated using the following equations:

$P=E/\Delta t$

$E = 0.5C(\Delta V)^2/3600M$

Where ΔV, Δt, M, and C are the potential window obtained from the discharge curve after the *IR* drop, discharge time, mass of the electrodes (in kg), and measured capacitance, respectively.

3. Results and discussion

Monolithic hierarchically porous carbons based on a PIM were prepared via the following steps: PIM synthesis, fabrication of a hierarchically structured polymer film, and carbonization of the film. First, the shape-persistent ladder polymer PIM-EA-TB was synthesized via the polymerization of ethanoanthracene (EA) by the formation of Tröger's base (TB) linking groups. The polymerization was monitored by ^{1}H NMR, FT-IR, and elemental analysis (Fig. S1). The molecular weight *(M_n)* of the polymer was found to be ca. 32700 *Da* using gel permeation chromatography. In order to obtain high-molecular-weight PIM-EA-TB, which is important to cast a mechanically robust polymer film, care should be taken to acquire high purity diamino-ethanoanthracene monomer. Meso- and macropores were formed in intrinsically microporous PIM-EA-TB via nonsolvent-induced phase separation (NIPS). A PIM-EA-TB solution in a mixture of DB and THF (1:4 w/w) was cast on a flat glass plate and then submerged in a methanol bath. Through the solvent/nonsolvent exchange process, a free-standing and hierarchically porous PIM-EA-TB film was formed (Fig. 1); the resulting opaque film was referred to as NPIM-EA-TB. The different solvent/nonsolvent exchange rates across the cross-section of PIM-EA-TB during the NIPS process induced the formation of many meso- and macropores. Specifically, a bicontinuous network structure with large open pores of 2 to 6 μm was observed on the top surface of NPIM-EA-TB, which was exposed to air, as seen in the upper SEM image, while the bottom of the film, which was in contact with the glass substrate during NIPS, was less porous. The entire film contained micropores originating from PIM-EA-TB, resulting in a hierarchical porous structure (Fig. S2 and S3). To fabricate hierarchically porous carbon monoliths, NPIM-EA-TB films were carbonized at 1100 °C; the resulting carbonized films were referred to as cNPIM-EA-TB_X, where X denotes the degree of

carbonization. Although carbonization reduced the area of the NPIM-EA-TB film by 25%, cross-sectional SEM images of cNPIM-EA-TB_80 (Fig. 1(c)) revealed that the hierarchically porous architecture with a pore size gradient in the surface normal direction was retained after carbonization.

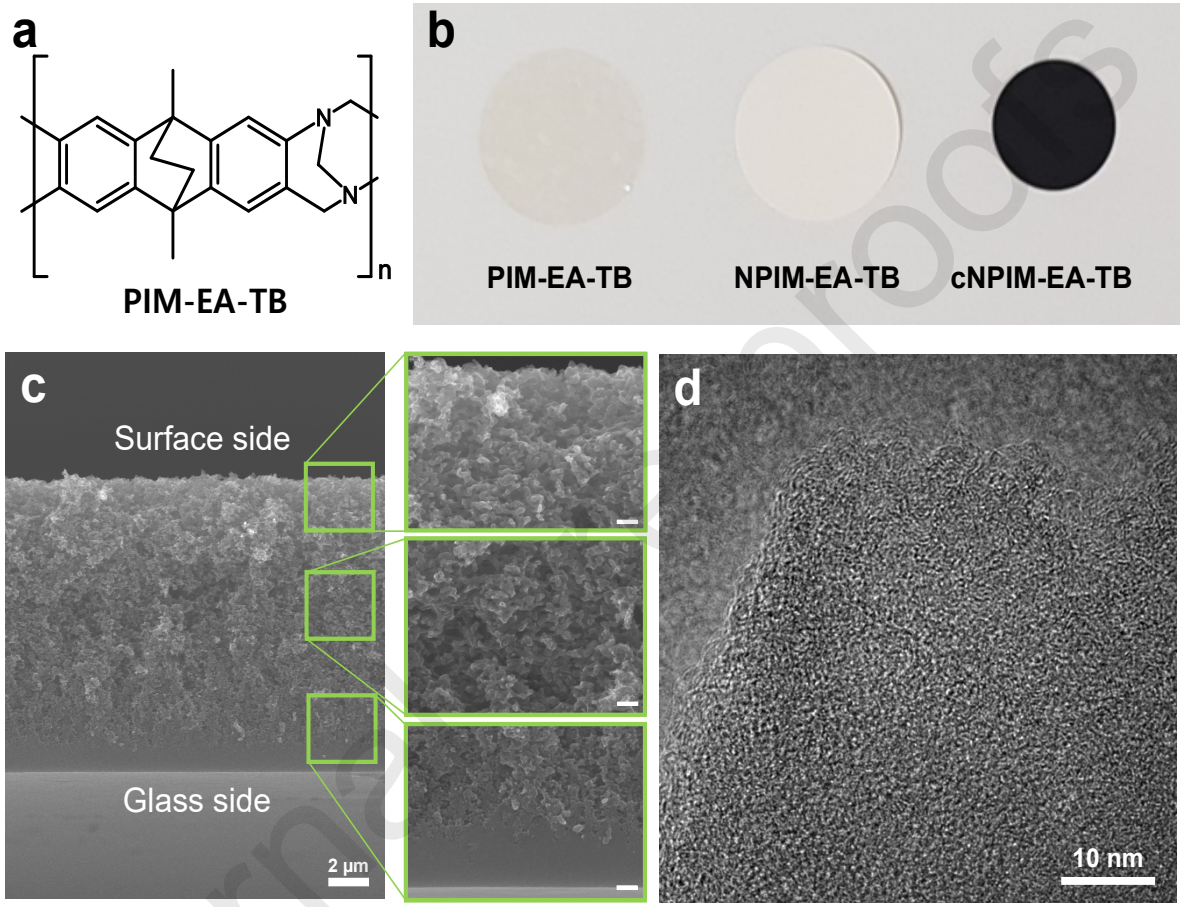

Fig. 1. (a) Chemical structure of PIM-EA-TB. (b) Photographs of the PIM-EA-TB, NPIM-EA-TB, and cNPIM-EA-TB_80 films. (c) SEM images of cNPIM-EA-TB_80 (Note: the scale bar in the magnified figures in the right column represents 500 nm). (d) TEM image of cNPIM-EA-TB_80.

To investigate the porous structure of cNPIM-EA-TB, sorption measurements were conducted using N_2 as the probe gas at 77 K (Table 1 and Fig. 2). The specific surface area and pore volume of cNPIM-EA-TB increased with increasing the holding time (120 vs. 180 min) during carbonization at 1100 °C, resulted in a degree of carbonisation of 70 and 80 wt%, respectively. It is noteworthy that cNPIM-EA-TB_80 exhibits a high BET surface area of 1966 m^2 g^{-1} and pore volume of 1.085 cm^3 g^{-1}. This surface area value is comparable to the most porous commercial activated carbons and almost twice as high as that of the pristine PIM-EA-TB precursor. The nitrogen sorption isotherms of cNPIM-EA-TB_70 and cNPIM-EA-TB_80 were type-I/IV, indicating that these carbon materials were hierarchically porous, containing both micropores (as indicated by the steep increase in adsorption at a low relative pressure) and meso- and macropores (as indicated by the linear and finally convex shape of the curve at higher relative pressure). Notably, the hysteresis often observed for PIMs between the N_2 adsorption and desorption curves is absent. The results demonstrate that cNPIM-EA-TB retains its enhanced microporosity, centered at a pore diameter of 0.74 nm and exhibited a narrow pore size distribution (PSD), after carbonization, while other pore development

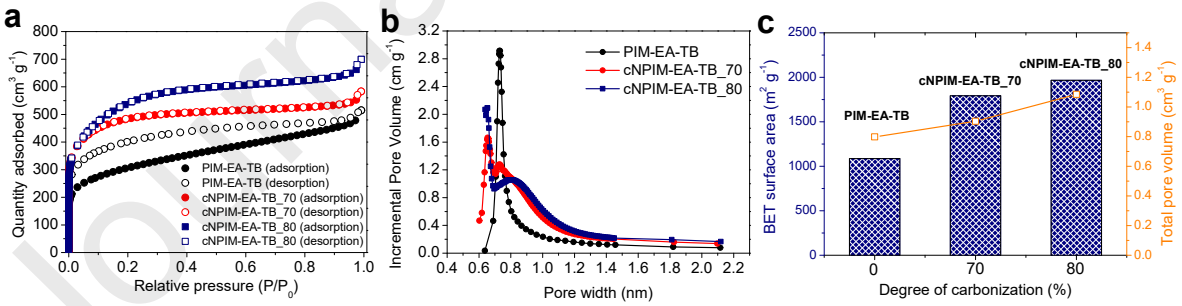

Fig. 2. (a) N_2 adsorption (filled circles)–desorption (open circles) isotherms, (b) pore size distribution of the micropores, and (c) BET surface area (m^2 g^{-1}) and total pore volume (cm^3 g^{-1}) as a function of the degree of carbonization (%) for cPIM-EA-TB with 0, 70, and 80% degree of carbonization.

processes such as the activation method can result in a broadened PSD. For cNPIM-EA-TB_80, the micropore (d < 2 nm) volume was 0.893 $cm^3 g^{-1}$, while those of the mesopores (2 < d < 50 nm) and macropores (300 nm > d > 50 nm) were both 0.192 $cm^3 g^{-1}$ (Table 1). These observations indicated that cNPIM-EA-TB_80 possesses a hierarchical structure, with micropores, centered at 0.74 nm, and large meso- and macropore volumes induced by the NIPS process.

Table 1. Pore characteristics of cNPIM-EA-TB_70 and cNPIM-EA-TB_80

	S_{BET} ($m^2 g^{-1}$)	S_{micro} ($m^2 g^{-1}$)[a]	V_{total} ($cm^3 g^{-1}$)[b]	V_{micro} ($cm^3 g^{-1}$)[a]
PIM-EA-TB	1090.2	1057.7	0.658	0.596
cNPIM-EA-TB_70	1793.9	1750.6	0.904	0.769
cNPIM-EA-TB_80	1966.1	1897.0	1.085	0.893

[a] Micropore surface area and volume calculated using the t-plot method. [b] Total pore volume.

The chemical composition and structure of cNPIM-EA-TB were characterized using X-ray photoelectron spectroscopy (XPS), EDS analysis, XRD spectroscopy,and Raman spectroscopy (Fig. 3). The XPS data for cNPIM-EA-TB_80 indicate that the atomic composition of the surface was 98.59% C and 1.41% O, which was consistent with EDS analysis results, revealing that cNPIM-EA-TB_80 sample was a carbon material with well distributed small portion of oxygen atoms (Fig. S4).These results showed that the nitrogen atoms of PIM-EA-TB were removed completely during carbonization, and that the carbonized PIM-EA-TB consisted mainly of carbon atoms. In addition, XRD analysis showed that the

characteristic peaks of both cNPIM-EA-TB 70 and 80 were positioned at 2 θ = 23° and 43°, corresponding to the reflections of the broad (002) and (100) planes, respectively, indicating that both cNPIM-EA-TB 70 and 80 samples were amorphous carbon (Fig. S5). Further, the molecular structure of the material was characterized using Raman spectroscopy. The two prominent peaks at 1350 and 1580 cm^{-1} corresponded to the D and G bands, which represent disordered and graphitic structures, respectively. The intensities of these bands indicated that the carbonized PIM-EA-TB had a disordered microstructure [36]. The ratios of the intensity of the D-band (I_D) to the G-band intensity (I_G) for cNPIM-EA-TB_70 and cNPIM-EA-TB_80 were 1.30 and 1.35, respectively. The C 1s XPS spectra of cNPIM-EA-TB_70 and 80 were deconvoluted into five spectral peaks corresponding to sp^2 carbon, sp^3 carbon, C-O bonds (hydroxyl and epoxy), C=O bonds (carbonyl), and O-C=O bonds (carboxyl) [37, 38]. Although the cNPIM-EA-TB samples contained oxygen-containing functional groups, such as hydroxyl and carbonyl groups, these were present in small amounts, as the samples contained less than 2 wt% oxygen. Consequently, the cNPIM-EA-TB samples consisted mainly of carbon atoms, making them suitable as electrodes for electrical double layer-capacitor (EDLC)-type SCs.

In electrical double layer-capacitor (EDLC) type super capacitors, high-surface-area and high-electrical-conductivity electrodes are the primary requirement for superior SC performance [4]. The electrical conductivity of the carbonized PIM-EA-TB was investigated using a four-point probe system, and found to be 148 S cm^{-1} for cNPIM-EA-TB_70 and 83.6 S cm^{-1} for cNPIM-EA-TB_80, respectively. The specific surface area and electrical conductivity of cNPIM-EA-TB_80 exceeded those of a number of notable examples in the literature, and were comparable

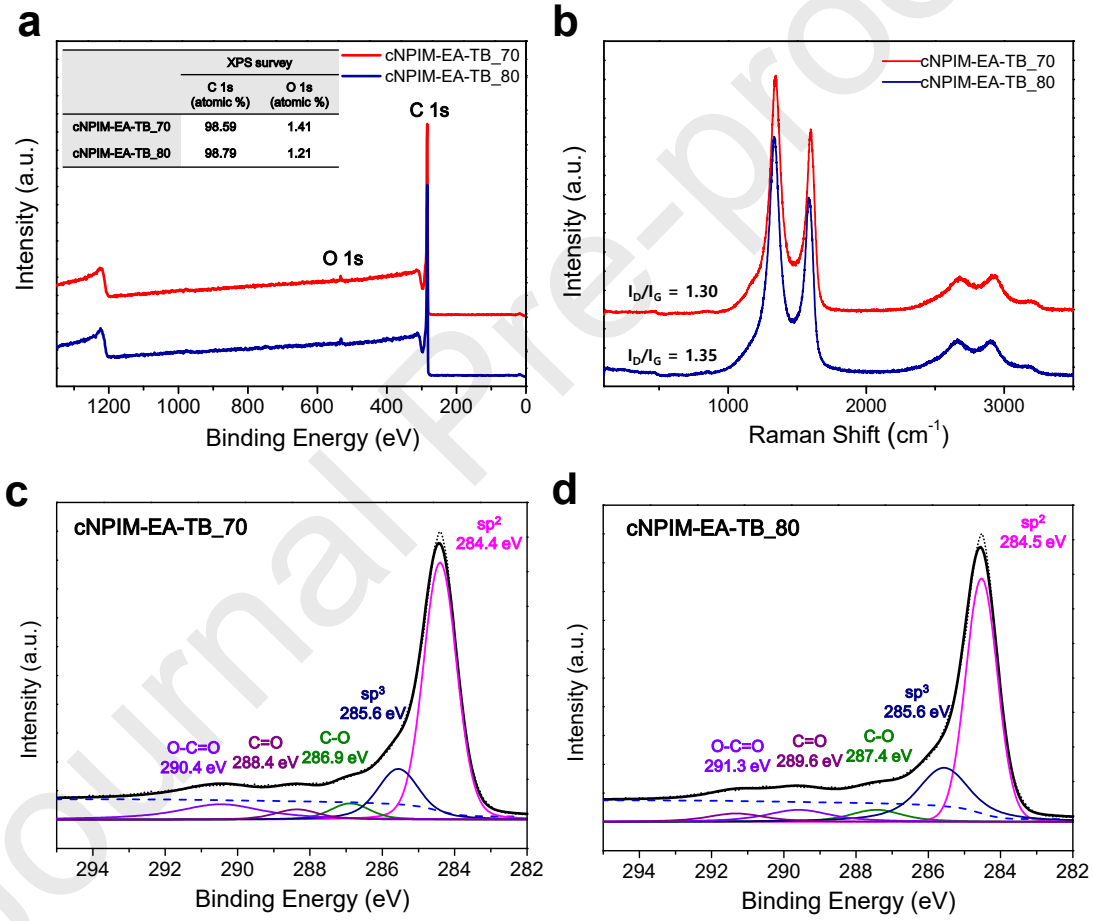

Fig. 3. (a) XPS survey scan and (b) Raman spectra of cNPIM-EA-TB_70 and cNPIM-EA-TB_80. Deconvoluted C 1s XPS spectra of (c) cNPIM-EA-TB_70 and (d) cNPIM-EA-TB_80.

to those of carbonized PIM-1 (Table S1) [16, 25, 39-41].

The electrochemical properties of the cNPIM-EA-TB_70 and cNPIM-EA-TB_80 electrodes were evaluated using cyclic voltammetry (CV) and galvanostatic charge-discharge (GCD) measurements in two-electrode mode. Fig. 4a and S6 show the CV curves of the cNPIM-EA-TB_80 and 70 electrodes obtained by varying the voltage from 0 to 2.5 V at a constant scan rate of 50 mV s^{-1}; no evident polarization was observed over the tested voltage window. A wide voltage window is particularly important for SCs, because energy density is proportional to the square of the voltage window according to the equation E=0.5CV^2 [4]. The nearly rectangular CV curves indicated that the electrodes showed purely capacitive behavior [42]. Although the box-like shape of the CV curve at 10 mV s^{-1} was slightly distorted as the scan rate was increased due to the limited ion diffusion, its capacitive features were retained even at the very high scan rate of 1000 mV s^{-1}, demonstrating good charge propagation across the electrodes (Fig. S7a,b) [43]. Interestingly, the current accumulated by the formation of electrode double layers (EDLs) for the cNPIM-EA-TB_80 electrode was more significant than for the cNPIM-EA-TB_70 electrode, presumably due to the larger surface area of the former electrode (Fig. S8). The capacitive features of the cNPIM-EA-TB electrodes were further confirmed by performing GCD measurements over the current range of 0.88 to 12 A g^{-1} (Fig. 4b and S7c,d). The triangular charge–discharge profiles indicated ideal capacitive behavior, consistent with the CV results. The charge/discharge duration of the cNPIM-EA-TB electrodes increased with increasing degree of carbonization at a specific current of 1 A g^{-1}. The corresponding specific capacitances were 41 and 46 F g^{-1} for cNPIM-EA-TB_70, and _80, respectively. Additionally, cNPIM-EA-TB_80 retained 73% of its low-current capacitance at a high specific current of 12 A g^{-1}, demonstrating its excellent rate-retention capability (Fig. 4c). The good electrochemical

properties of the cNPIM-EA-TB_80 electrode were attributed to its large surface area, which could contribute to the formation of EDLs and high electrical conductivity. This speculation was corroborated by EIS measurements over the frequency range 10^6–1 Hz. Fig. 4d shows the Nyquist plots of the cNPIM-EA-TB_70 and _80 electrodes. The equivalent series resistance (ESR) that appears at the intercept of the *x*-axis (the so-called real part) of the Nyquist plot is associated with the electrode resistance, electrolyte resistance, and contact resistance between the current collector and electrode [44, 45]. The ESRs of cNPIM-EA-TB_70 and _80 were 2.9 and 2.6 Ω, respectively. These results demonstrated that the pore creation process using NIPS followed by carbonization did not have a detrimental effect on the electric properties of the PIM electrode. The semicircle in the high-frequency to mid-frequency region of the Nyquist plot was attributed to interfacial charge transfer resistance (R_{CT})[42]. The higher degree of carbonization of cNPIM-EA-TB_80 resulted in a smaller R_{CT} (25 Ω) than that of cNPIM-EA-TB_70 (42 Ω). The nearly vertical slope of the PIM-based materials in the low-frequency region also indicates ideal capacitive behavior.

The cycle life of the cNPIM-EA-TB_80 electrode was estimated by using 10000 GCD cycles at a constant specific current of 1.7 A g^{-1} (Fig. 4e). Notably, 90% of the specific capacitance during the first cycle was preserved after 10000 GCD cycles. No columbic efficiency fading and morphological change were also observed at the end of the test (Fig. S9). Fig. 4f shows the Ragone plots of the PIM-based electrodes; their energy density was ~17 Wh kg^{-1} at a power density of 1 kW kg^{-1}. This value exceeds or is comparable to the energy densities of state-of-the-art SCs (Table S2) [46-52]. The good capacitive and electrical properties of cNPIM-EA-TB electrodes are attributed to its 3D porous hierarchical structure. The macropores of the hierarchical structure are mostly filled by electrolytes and form continuous

phase, acting as ion-buffering reservoirs. Via the mesopores that seamlessly bridge the gap between macro- and micropores, the electrolyte ions can reach to micropores that play a primarily role in providing exceptional specific surface area of 1966 m^2 g^{-1}. The electrons can also transport through continuous phase of cNPIM-EA-TB framework, leading to a good electrical conductivity.

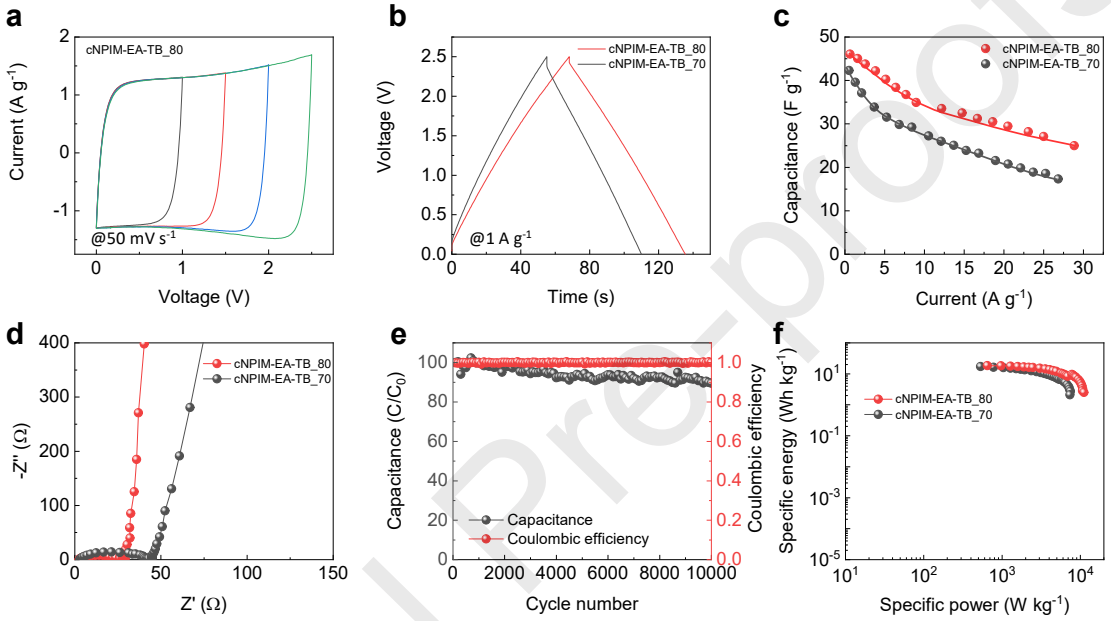

Fig. 4. (a) CV curves of cNPIM-EA-TB_80 electrodes at a scan rate of 50 mV s^{-1} over the voltage window of 0 to 2.5 V. (b) GCD profiles (at 1 A g^{-1}), (c) rate-retention capability, and (d) Nyquist plots of the cNPIM-EA-TB_70 and _80 electrodes. (e) Long-term cycle stability of the cNPIM-EA-TB_80 electrodes over 10000 GCD cycles at a constant current of 1.7 A g^{-1}. C_0 is the initial capacitance and C is the capacitance at the indicated number of cycles. (f) The Ragone plots of the cNPIM-EA-TB based electrode.

4. Conclusions

Starting from the intrinsically microporous polymer PIM-EA-TB, we successfully prepared hierarchically structured carbon electrodes (cNPIM-EA-TB) for high-performance SCs. The hierarchically porous carbon materials were fabricated by the synthesis of PIM-EA-TB, NIPS processing of a PIM-EA-TB solution, and subsequent carbonization of the resulting films.

Notably, the use of an intrinsically microporous polymer ensures that the resulting carbon materials have both high surface area and electrical conductivity, while preserving their initial microporous architecture. The cPIM-EA-TB electrodes showed excellent SC performance with a high specific capacitance, good rate-retention capability, and good specific energy and power. Thus, PIM-EA-TB represents a promising new precursor material for the preparation of 3D hierarchically structured carbon materials for energy and environmental applications.

Acknowledgements

J. W. Jeon. and J. Shin contributed equally to this work. This work was supported by the Korea Research Institute of Chemical Technology (KRICT) core project (KK1607-C06, KK1961-02, and SI1921-20) and the Materials and Components Technology Development Program (no. 10062226) funded by the Ministry of Trade, Industry&Energy (MOTIE/KEIT, Korea) and Basic Science Research Program through the National Research Foundation of Korea (NRF) funded by the Ministry of Education (No. NRF-2018R1D1A3B07048748).

References

[1] J.R. Miller, P. Simon, Electrochemical capacitors for energy management, Science, 321 (2008) 651-652.

[2] J.R. Miller, P. Simon, Fundamentals of electrochemical capacitor design and operation, Electrochem. Soc. Interface, 17 (2008) 31-32.

[3] B. Dunn, H. Kamath, J.-M. Tarascon, Electrical energy storage for the grid: a battery of

choices, Science, 334 (2011) 928-935.

[4] P. Simon, Y. Gogotsi, Materials for electrochemical capacitors, Nat. Mater., 7 (2008) 845-854.

[5] A. González, E. Goikolea, J.A. Barrena, R. Mysyk, Review on supercapacitors: technologies and materials, Renewable Sustainable Energy Rev., 58 (2016) 1189-1206.

[6] D. Zhao, K. Jiang, J. Li, X. Zhu, C. Ke, S. Han, E. Kymakis, X. Zhuang, Supercapacitors with alternating current line-filtering performance, BMC Materials, 2 (2020) 3.

[7] D. Zhao, W. Chang, C. Lu, C. Yang, K. Jiang, X. Chang, H. Lin, F. Zhang, S. Han, Z. Hou, Charge transfer salt and graphene heterostructure-based micro-supercapacitors with alternating current line-filtering performance, Small, 15 (2019) 1901494.

[8] K. Jiang, I.A. Baburin, P. Han, C. Yang, X. Fu, Y. Yao, J. Li, E. Cánovas, G. Seifert, J. Chen, Interfacial Approach toward Benzene-Bridged Polypyrrole Film–Based Micro-Supercapacitors with Ultrahigh Volumetric Power Density, Adv. Funct. Mater., 30 (2020) 1908243.

[9] R. Kötz, M. Carlen, Principles and applications of electrochemical capacitors, Electrochim. Acta, 45 (2000) 2483-2498.

[10] A. Pandolfo, A. Hollenkamp, Carbon properties and their role in supercapacitors, J. Power Sources, 157 (2006) 11-27.

[11] G. Wang, L. Zhang, J. Zhang, A review of electrode materials for electrochemical supercapacitors, Chem. Soc. Rev., 41 (2012) 797-828.

[12] Z. Yang, J. Tian, Z. Yin, C. Cui, W. Qian, F. Wei, Carbon nanotube-and graphene-based nanomaterials and applications in high-voltage supercapacitor: A review, Carbon, 141 (2019) 467-480.

[13] R. Dubey, V. Guruviah, Review of carbon-based electrode materials for supercapacitor energy storage, Ionics, 25 (2019) 1419-1445.

[14] T. Liu, F. Zhang, Y. Song, Y. Li, Revitalizing carbon supercapacitor electrodes with hierarchical porous structures, J. Mater. Chem. A, 5 (2017) 17705-17733.

[15] C. Cheng, S. He, C. Zhang, C. Du, W. Chen, High-performance supercapacitor fabricated from 3D free-standing hierarchical carbon foam-supported two dimensional porous thin carbon nanosheets, Electrochim. Acta, 290 (2018) 98-108.

[16] J.W. Jeon, J.H. Han, S.-K. Kim, D.-G. Kim, Y.S. Kim, D.H. Suh, Y.T. Hong, T.-H. Kim, B.G. Kim, Intrinsically microporous polymer-based hierarchical nanostructuring of electrodes via nonsolvent-induced phase separation for high-performance supercapacitors, J. Mater. Chem. A, 6 (2018) 8909-8915.

[17] J. Yang, H. Wu, M. Zhu, W. Ren, Y. Lin, H. Chen, F. Pan, Optimized mesopores enabling enhanced rate performance in novel ultrahigh surface area meso-/microporous carbon for supercapacitors, Nano Energy, 33 (2017) 453-461.

[18] F. Wang, X. Wu, X. Yuan, Z. Liu, Y. Zhang, L. Fu, Y. Zhu, Q. Zhou, Y. Wu, W. Huang, Latest advances in supercapacitors: from new electrode materials to novel device designs, Chem. Soc. Rev., 46 (2017) 6816-6854.

[19] R.T. Woodward, F. Markoulidis, F. De Luca, D.B. Anthony, D. Malko, T.O. McDonald, M.S.P. Shaffer, A. Bismarck, Carbon foams from emulsion-templated reduced graphene oxide polymer composites: Electrodes for supercapacitor devices, J. Mater. Chem. A, 6 (2017) 1840-1849.

[20] U.N. Maiti, J. Lim, K.E. Lee, W.J. Lee, S.O. Kim, Three-dimensional shape engineered, interfacial gelation of reduced graphene oxide for high rate, large capacity supercapacitors,

Adv. Mater., 26 (2014) 615-619.

[21] D. Puthusseri, V. Aravindan, S. Madhavi, S. Ogale, 3D micro-porous conducting carbon beehive by single step polymer carbonization for high performance supercapacitors: the magic of in situ porogen formation, Energy Environ. Sci., 7 (2014) 728-735.

[22] Z. Yu, L. Tetard, L. Zhai, J. Thomas, Supercapacitor electrode materials: nanostructures from 0 to 3 dimensions, Energy Environ. Sci., 8 (2015) 702-730.

[23] M. Rose, Y. Korenblit, E. Kockrick, L. Borchardt, M. Oschatz, S. Kaskel, G. Yushin, Hierarchical Micro-and Mesoporous Carbide-Derived Carbon as a High-Performance Electrode Material in Supercapacitors, Small, 7 (2011) 1108-1117.

[24] Y. Zhu, S. Murali, M.D. Stoller, K. Ganesh, W. Cai, P.J. Ferreira, A. Pirkle, R.M. Wallace, K.A. Cychosz, M. Thommes, Carbon-based supercapacitors produced by activation of graphene, Science, 332 (2011) 1537-1541.

[25] Y. Xu, Z. Lin, X. Zhong, X. Huang, N.O. Weiss, Y. Huang, X. Duan, Holey graphene frameworks for highly efficient capacitive energy storage, Nat. Commun., 5 (2014) 4554.

[26] F. Marken, E. Madrid, Y. Zhao, M. Carta, N.B. McKeown, Polymers of Intrinsic Microporosity (PIMs) in Triphasic Electrochemistry: Perspectives, ChemElectroChem, 6 (2019) 4332-4342.

[27] P.M. Budd, E.S. Elabas, B.S. Ghanem, S. Makhseed, N.B. McKeown, K.J. Msayib, C.E. Tattershall, D. Wang, Solution-processed, organophilic membrane derived from a polymer of intrinsic microporosity, Adv. Mater., 16 (2004) 456-459.

[28] N.B. McKeown, Polymers of intrinsic microporosity, ISRN Mater. Sci., 2012 (2012) 1-16.

[29] S.-Y. Son, Y.-J. Noh, C. Bock, S. Lee, B.G. Kim, S.-I. Na, H.-I. Joh, One-step synthesis

of carbon nanosheets converted from a polycyclic compound and their direct use as transparent electrodes of ITO-free organic solar cells, Nanoscale, 6 (2014) 678-682.

[30] J.S. Bonso, G.D. Kalaw, J.P. Ferraris, High surface area carbon nanofibers derived from electrospun PIM-1 for energy storage applications, J. Mater. Chem. A, 2 (2014) 418-424.

[31] Y. Rong, D. He, A. Sanchez-Fernandez, C. Evans, K.J. Edler, R. Malpass-Evans, M. Carta, N.B. McKeown, T.J. Clarke, S.H. Taylor, Intrinsically microporous polymer retains porosity in vacuum thermolysis to electroactive heterocarbon, Langmuir, 31 (2015) 12300-12306.

[32] M. Carta, R. Malpass-Evans, M. Croad, Y. Rogan, J.C. Jansen, P. Bernardo, F. Bazzarelli, N.B. McKeown, An efficient polymer molecular sieve for membrane gas separations, Science, 339 (2013) 303-307.

[33] E. Madrid, Y. Rong, M. Carta, N.B. McKeown, R. Malpass-Evans, G.A. Attard, T.J. Clarke, S.H. Taylor, Y.T. Long, F. Marken, Metastable Ionic Diodes Derived from an Amine-Based Polymer of Intrinsic Microporosity, Angew. Chem. Int. Ed., 53 (2014) 10751-10754.

[34] E. Madrid, P. Cottis, Y. Rong, A.T. Rogers, J.M. Stone, R. Malpass-Evans, M. Carta, N.B. McKeown, F. Marken, Water desalination concept using an ionic rectifier based on a polymer of intrinsic microporosity (PIM), J. Mater. Chem. A, 3 (2015) 15849-15853.

[35] Y. Rong, R. Malpass-Evans, M. Carta, N.B. McKeown, G.A. Attard, F. Marken, High density heterogenisation of molecular electrocatalysts in a rigid intrinsically microporous polymer host, Electrochem. Commun., 46 (2014) 26-29.

[36] M. Heon, S. Lofland, J. Applegate, R. Nolte, E. Cortes, J.D. Hettinger, P.-L. Taberna, P. Simon, P. Huang, M. Brunet, Continuous carbide-derived carbon films with high volumetric capacitance, Energy Environ. Sci., 4 (2011) 135-138.

[37] O.C. Compton, B. Jain, D.A. Dikin, A. Abouimrane, K. Amine, S.T. Nguyen, Chemically active reduced graphene oxide with tunable C/O ratios, ACS Nano, 5 (2011) 4380-4391.

[38] N.-F. Chiu, C.-D. Yang, C.-C. Chen, C.-T. Kuo, Stepwise control of reduction of graphene oxide and quantitative real-time evaluation of residual oxygen content using EC-SPR for a label-free electrochemical immunosensor, Sens. Actuators, B, 258 (2018) 981-990.

[39] M.F. El-Kady, V. Strong, S. Dubin, R.B. Kaner, Laser scribing of high-performance and flexible graphene-based electrochemical capacitors, Science, 335 (2012) 1326-1330.

[40] R. Chandrasekaran, Y. Soneda, J. Yamashita, M. Kodama, H. Hatori, Preparation and electrochemical performance of activated carbon thin films with polyethylene oxide-salt addition for electrochemical capacitor applications, J. Solid State Electrochem., 12 (2008) 1349-1355.

[41] D. Sheberla, J.C. Bachman, J.S. Elias, C.-J. Sun, Y. Shao-Horn, M. Dincă, Conductive MOF electrodes for stable supercapacitors with high areal capacitance, Nat. Mater., 16 (2017) 220-224.

[42] W. Chen, R. Rakhi, L. Hu, X. Xie, Y. Cui, H.N. Alshareef, High-performance nanostructured supercapacitors on a sponge, Nano Lett., 11 (2011) 5165-5172.

[43] S.K. Kim, H.J. Koo, A. Lee, P.V. Braun, Selective Wetting-Induced Micro-Electrode Patterning for Flexible Micro-Supercapacitors, Adv. Mater., 26 (2014) 5108-5112.

[44] J. Chmiola, G. Yushin, Y. Gogotsi, C. Portet, P. Simon, P.-L. Taberna, Anomalous increase in carbon capacitance at pore sizes less than 1 nanometer, Science, 313 (2006) 1760-1763.

[45] F. SuongáOu, Synthesis of hybrid nanowire arrays and their application as high power supercapacitor electrodes, Chem. Commun., (2008) 2373-2375.

[46] J. Xu, Q. Gao, Y. Zhang, Y. Tan, W. Tian, L. Zhu, L. Jiang, Preparing two-dimensional microporous carbon from Pistachio nutshell with high areal capacitance as supercapacitor materials, Sci. Rep., 4 (2014) 5545.

[47] J. Zhi, W. Zhao, X. Liu, A. Chen, Z. Liu, F. Huang, Highly conductive ordered mesoporous carbon based electrodes decorated by 3D graphene and 1D silver nanowire for flexible supercapacitor, Adv. Funct. Mater., 24 (2014) 2013-2019.

[48] F. Miao, C. Shao, X. Li, K. Wang, Y. Liu, Flexible solid-state supercapacitors based on freestanding nitrogen-doped porous carbon nanofibers derived from electrospun polyacrylonitrile@polyaniline nanofibers, J. Mater. Chem. A, 4 (2016) 4180-4187.

[49] Y. Qiu, G. Li, Y. Hou, Z. Pan, H. Li, W. Li, M. Liu, F. Ye, X. Yang, Y. Zhang, Vertically aligned carbon nanotubes on carbon nanofibers: a hierarchical three-dimensional carbon nanostructure for high-energy flexible supercapacitors, Chem. Mater., 27 (2015) 1194-1200.

[50] Y. Jiang, J. Yan, X. Wu, D. Shan, Q. Zhou, L. Jiang, D. Yang, Z. Fan, Facile synthesis of carbon nanofibers-bridged porous carbon nanosheets for high-performance supercapacitors, J. Power Sources, 307 (2016) 190-198.

[51] J. Xia, N. Zhang, S. Chong, Y. Chen, C. Sun, Three-dimensional porous graphene-like sheets synthesized from biocarbon via low-temperature graphitization for a supercapacitor, Green Chem., 20 (2018) 694-700.

[52] E.D. Walsh, X. Han, S.D. Lacey, J.-W. Kim, J.W. Connell, L. Hu, Y. Lin, Dry-processed, binder-free holey graphene electrodes for supercapacitors with ultrahigh areal loadings, ACS Appl. Mater. Interfaces, 8 (2016) 29478-29485.

Highlights

PIM-EA-TB based hierarchically structured carbon for supercapacitor electrodes.

Phase separation process introduces meso-&macro-pores into the microporous polymer.

The hierarchical structure is retained even after carbonization.

The resulting carbon shows a high surface area and a good electrical conductivity.

These characteristics gives it a high specific capacitance at a specific power.